Research Article Vol. 65, No. 26 / 10 September 2026 / Applied Optics 8943

applied optics

High-efficiency direct in-band pumping of Tm:LuAG with a 1 W single-emitter diode

Hatice Bilici,[1] Fatma Kaya,[1] Umit Demirbas,[2,3] and Ersen Beyatli[1,*]

[1]Department of Electrical-Electronics Engineering, Recep Tayyip Erdogan University, Rize 53100, Turkey
[2]Laser Technology Laboratory, Department of Electrical and Electronics Engineering, Antalya Bilim University, Antalya 07190, Turkey
[3]Paul Scherrer Institute, Villigen PSI CH-5232, Switzerland
*ersen.beyatli@erdogan.edu.tr

Received 22 June 2026; revised 9 August 2026; accepted 11 August 2026; posted 12 August 2026; published 1 September 2026

We demonstrate a compact and efficient Tm:LuAG laser operating at 2023 nm, directly in-band pumped at 1621 nm by a high-brightness 1 W single-emitter diode. Five crystals with 4% and 6% Tm^{3+} doping and lengths of 3–7 mm were compared in the same X-fold resonator. In continuous-wave (CW) operation, the 4%, 7 mm crystal produced 147 mW at 10°C with a local absorbed-pump slope efficiency reaching 76.6%. Comparison of the five crystals showed that the benefit of increased pump absorption with crystal length was eventually offset by reabsorption and passive loss, particularly at the higher Tm^{3+} concentration. The optimum crystal also maintained good spatial beam quality, with average M^2 values of 1.58 and 1.03 along the horizontal and vertical axes, respectively. The same platform provided 138 nm of continuous tuning from 1937 to 2075 nm, stable two- and three-line emission, and SESAM-based passive Q-switching, with pulse durations down to 2 μs, peak powers up to 564 mW, and pulse energies up to 1.42 μJ. To our knowledge, the measured absorbed-pump slope efficiency is the highest reported for a directly diode-pumped CW Tm:LuAG laser. © 2026 Optica Publishing Group. All rights, including for text and data mining (TDM), Artificial Intelligence (AI) training, and similar technologies, are reserved.

https://doi.org/10.1364/AO.609261

1. INTRODUCTION

Solid-state lasers near 2 μm are attractive for coherent lidar, remote sensing, medical surgery, materials processing, and pumping mid-infrared OPOs because this region combines reduced retinal hazard, strong absorption by water and biological tissues, and overlap with atmospheric molecular absorption lines [1–6]. For practical use, these sources should also ideally combine compact direct-diode pumping with high efficiency, good beam quality, thermal stability, wavelength tunability, and access to both CW and pulsed operation.

Tm^{3+} ions provide ~2 μm laser emission through the $^3F_4 \rightarrow {}^3H_6$ transition. In the conventional ~790 nm pumping scheme, excitation of the $^3H_6 \rightarrow {}^3H_4$ band enables cross relaxation, so that one absorbed pump photon can populate two ions in the $^3F_4$ upper laser level [7–10]. This two-for-one process can produce slope efficiencies above the Stokes limit; however, efficient cross relaxation generally requires relatively high Tm^{3+} concentrations, which can increase concentration-dependent loss, reabsorption, and thermal loading, thereby constraining the usable doping range [11,12]. Thus, pump absorption, cross-relaxation efficiency, thermal loading, and dopant concentration are intrinsically coupled in conventionally pumped Tm lasers. In-band pumping at ~1.6−1.7 μm directly excites the $^3H_6 \rightarrow {}^3F_4$ upper laser level, reducing the quantum defect to approximately 15%–20% and enabling efficient operation with substantially lower thermal loading [12]. Because this scheme does not rely on cross relaxation, the Tm^{3+} concentration and crystal length can be selected more freely to balance pump absorption, reabsorption, passive loss, and thermal robustness [12]. In-band pumping has been successfully applied to a broad range of Tm-doped crystalline hosts, establishing it as a general route to efficient 2 μm laser operation [12–21]. Representative performance benchmarks are summarized in Table 1.

Among Tm^{3+}-doped hosts, LuAG is particularly attractive because it combines the mechanical robustness and favorable thermal properties of garnets with useful spectroscopic characteristics [26]. Compared with YAG, LuAG offers a relatively small ionic-radius mismatch between Tm^{3+} and Lu^{3+}, strong Stark splitting of the Tm^{3+} manifolds, and a long $^3F_4$ upper-state lifetime, supporting efficient 2 μm operation and energy storage for pulsed regimes [27,28]. These favorable material properties have enabled Tm:LuAG operation across a wide range of CW and pulsed regimes.

Under conventional short-wavelength pumping, primarily near 790 nm but also at 681 nm, Tm:LuAG lasers have reached CW output powers of 8.5 W with a slope efficiency of 44.5% [29], while high-brightness 681 nm tapered-diode pumping produced 295 mW with slope efficiencies approaching 51% [30]. In pulsed operation, active and passive Q-switching have produced sub-100-ns pulses and pulse energies exceeding 10 mJ

Table 1. Comparison of the Present Work (*) with Representative In-Band-Pumped Tm-Doped Laser Results

Host	Pump	P_{out} (W)	η (%)	Reference
Tm:KYW	LD (2 W, 1750 nm)	0.086	28	[13]
	LD (15 W, 1720 nm)	4.55	83	[14]
Tm:YLF	Er:fiber and Raman (2.5 W, 1678 nm)	0.46	50	[15]
	LD (30 W, 1700 nm)	6.4	85	[12]
Tm:YAG	Er:YAG (12.8 W, 1617 nm)	7.3	62.3	[16]
	LD (30 W, 1700 nm)	6.5	68	[12]
Tm:$CaYAlO_4$	Raman fiber laser (14 W, 1704 nm)	6.8	52.3	[17]
Tm:Y_2O_3	Raman fiber laser (14.1 W, 1620 nm)	5.5	53	[22]
Tm:Sc_2O_3	Er:Yb fiber (8 W, 1611 nm)	1	47	[18]
Tm:Lu_2O_3	2 × LD (2 × 20 W, 1725 nm)	6.1	66.4	[19]
	LD (20 W, 1725 nm)	3.3	64.9	[20]
Tm:CaF_2	Er-Yb fiber (2.6 W, 1610 nm)	1.25	55	[21]
Tm:YAP	LD (30 W, 1700 nm)	8.7	80	[12]
Tm:LuAG	LD (10 W, 1600 nm)	2.3	33.4	[23]
	OPO (20 W, 1623 nm)	10.8	60.5	[24]
	LD (30 W, 1711 nm)	7.26	38.5	[25]
	LD (1 W, 1621 nm)	0.147	64.6/76.6	*

[29,31–33], while Q-switched mode-locking and SESAM-based mode locking have extended Tm:LuAG operation into the picosecond regime [34–36]. Collectively, these results establish Tm:LuAG as a mature and versatile 2 μm gain medium supporting efficient CW, single-frequency, high-energy Q-switched, and mode-locked operation.

In-band-pumped Tm lasers have also progressed to watt-level CW and actively Q-switched operation. Direct pumping with a 9.5 W fiber-coupled diode near 1.6 μm produced 2.3 W of CW output with a slope efficiency of 33.4% [23]. More recently, OPO pumping at 1623 nm yielded 10.8 W with a slope efficiency of 60.5%, together with electro-optically Q-switched pulses of 8.14 mJ and 32 ns, corresponding to a peak power of 254 kW [24]. Direct diode pumping at 1711 nm also generated 7.26 W of CW output with a slope efficiency of 38.5% and acousto-optically Q-switched pulses of 5.63 mJ and 77 ns [25]. These results establish the power-scaling potential of in-band-pumped Tm, although the demonstrated systems employed high-power fiber-coupled diodes or laser-based pump sources.

Despite these advances, direct in-band pumping of Tm lasers with low-power, high-brightness single-emitter diodes has received relatively little attention. Although these diodes provide less pump power than fiber-coupled or laser-based pump sources, they enable a simpler and more compact pumping arrangement with tight focusing and efficient pump-to-cavity mode matching. Their high brightness may also be useful for future Kerr-lens mode-locking studies, where pump focusing and spatial mode overlap are critical.

In this work, we demonstrate a compact in-band-pumped Tm:LuAG laser directly driven by a low-cost 1 W single-emitter diode operating near 1621 nm. Five crystals with 4% and 6% Tm^{3+} doping and lengths of 3–7 mm were compared in the same X-fold resonator to determine how crystal length and concentration affect laser performance. Despite the modest pump power and simple architecture, the system produced CW output powers approaching 150 mW with absorbed-pump slope efficiencies reaching 76.6%, while also providing 138 nm of continuous wavelength tuning, stable two- and three-line emission, and SESAM-based passive Q-switching. These results demonstrate that a compact and inexpensive single-emitter pump architecture can support multiple CW and pulsed operating regimes rather than serving only as a basic low-power oscillator. To our knowledge, the system also achieves the highest slope efficiency reported for a directly diode-pumped CW Tm:LuAG laser.

2. EXPERIMENTAL SETUP

The experimental setup is shown schematically in Fig. 1. The pump source was a C-mount, single-emitter LDX Optronics H0116-1 laser diode with a 150 μm stripe width, a nominal emission wavelength of 1620 nm, and a maximum output power of 1 W. It directly excited the $^3H_6 \rightarrow {}^3F_4$ absorption band of Tm^{3+}. At a diode temperature of 20°C, the diode had a threshold current of 1.02 A and a slope efficiency of 0.237 W/A. At the rated 1 W operating point, the drive current and voltage were 5.9 A and 1.25 V, respectively. The emission wavelength increased with drive current and reached approximately 1621 nm near maximum power, with a spectral bandwidth of ∼8 nm FWHM. The diode operating temperature was experimentally optimized to obtain the best spectral overlap between the pump emission and the Tm:LuAG absorption feature near 1623 nm (FWHM: ∼6 nm) [23]. Although the present broad-area diode provided efficient pumping, the spectral overlap could be further improved using a wavelength-stabilized diode module centered near the stronger Tm:LuAG absorption peak at approximately 1634 nm (FWHM: ∼5 nm) [23]. A pump linewidth substantially narrower than this absorption feature, for example, ∼2 nm FWHM, would increase the pump-spectrum-weighted absorption and reduce current- and temperature-dependent variations in the absorbed pump fraction.

The measured pump-beam quality factors were $M^2 = 1.1$ along the fast vertical axis and $M^2 = 15$ along the slow axis. Using the beam-brightness definition $B = P/(M^2_{\text{fast}} M^2_{\text{slow}} \lambda^2)$

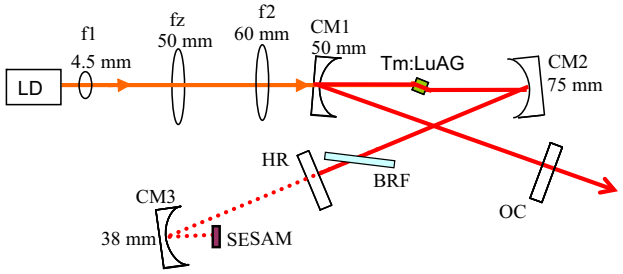

Fig. 1. Experimental setup of the in-band pumped Tm:LuAG laser system. LD, 1.62 μm laser diode; f1, 4.5 mm aspheric lens; fz, 5 cm cylindrical lens; f2, 6 cm achromatic lens; HR, flat high reflector; CM1–CM3, curved HR; OC, 1.3%.

in [37], these values correspond to a brightness of approximately 23 $mW/\mu m^2$ at the maximum output power of 1 W. The pump beam was collected and collimated by an aspheric lens ($f_1 = 4.51$ mm), while the different divergences along the fast and slow axes were compensated using a cylindrical lens ($f_z = 50$ mm). The beam was then focused into the gain crystal using an achromatic doublet ($f_2 = 60$ mm).

The laser resonator employed a four-mirror X-fold configuration. Two concave mirrors, CM1 (ROC = 50 mm) and CM2 (ROC = 75 mm), formed the folding section and defined the intracavity waist at the crystal position. CM1 also served as the pump input mirror, with high transmission at ∼1.6 μm and high reflectivity near ∼2 μm (R > 99.9%, 1850–2190 nm). The distances CM1–crystal center, crystal center–CM2, CM2–OC, and CM1–HR were approximately 34, 43, 242, and 165 mm, respectively, giving a total cavity length of approximately 480 mm in the CW configuration. An ABCD-matrix calculation yielded sagittal and tangential $1/e^2$ cavity-mode radii of approximately 20 and 36 μm, respectively, at the center of the gain crystal. The laser output was extracted through a flat 1.3% output coupler, while the opposite arm was terminated by a flat high reflector for CW operation. For passive Q-switching, the high reflector was replaced by CM3 (ROC: 37.5 mm), which focused the intracavity beam onto the SESAM.

Five Brewster-cut Tm:LuAG crystals, all with a nominal transverse aperture of 4 × 2 mm^2 (width × thickness), were investigated: 4% samples with lengths of 5 and 7 mm and 6% samples with lengths of 3, 5, and 7 mm, with corresponding pump absorption fractions of approximately 78%, 82%, 79%, 89%, and 96%, respectively. All crystals were mounted in a water-cooled copper heat sink. The Brewster-cut geometry minimized intracavity Fresnel losses for the p-polarized laser field and favored linearly polarized operation. For CW measurements, the cooling-water temperature was varied from 10 to 40°C. At each temperature, the output power was recorded as a function of absorbed pump power, from which the lasing threshold and slope efficiency were extracted. This procedure enabled a direct comparison of the effects of Tm^{3+} concentration, crystal length, and temperature under identical resonator conditions.

Wavelength tuning and multi-wavelength operation were studied by inserting an 8-mm-thick off-surface-optical-axis quartz birefringent filter (BRF) with a 25° cut angle into the OC arm of the cavity at Brewster's angle [38]. Its off-surface-axis geometry provides rotation-dependent transmission peaks with varying free spectral range and modulation depth. Rotating the BRF enabled continuous wavelength tuning across the gain bandwidth. At selected angles, two or three transmission peaks simultaneously satisfied the net-gain condition, enabling stable dual- and triple-wavelength operation.

Passive Q-switching experiments were performed at a water temperature of 15°C using the CM3–SESAM end arm. The estimated cavity-mode radius on the SESAM was ∼60 μm. The SESAM was specified for operation near 2 μm and had a modulation depth of 1.2%, a non-saturable loss of 0.8%, a saturation fluence of 70 $\mu J/cm^2$, and a recovery time of ∼10 ps.

3. RESULTS

A. Crystal-Length and Doping-Concentration Dependence of CW Lasing Performance

Figure 2 shows the measured CW output power as a function of absorbed pump power for all five Tm crystals at a water-cooling temperature of 10°C, obtained in free-running operation with a 1.3% output coupler. The free-running laser wavelength was around 2023 nm for all crystals. The corresponding thresholds, slope efficiencies, and maximum output powers at water temperatures of 10, 15, 20, and 25°C are summarized in Table 2. All input–output curves show a modest slope near threshold, followed by a progressively steeper increase with absorbed pump power. This curvature is characteristic of the quasi-three-level $^3F_4 \rightarrow {}^3H_6$ transition, as increasing population inversion progressively reduces ground-state reabsorption. To account for this behavior, the overall slope efficiency was obtained from a least-squares fit to the complete above-threshold dataset, whereas the high-power slope efficiency was determined from a separate fit to the approximately linear upper-power region, excluding the first two to four near-threshold points depending on the dataset.

As seen in Fig. 2 and Table 2, the lowest absorbed lasing threshold, 486 mW, was obtained with the 4%, 5 mm crystal, whereas the highest threshold, 587 mW, was measured for the 6%, 7 mm crystal. The remaining samples fall between these limits, showing a general increase in threshold with crystal length and Tm^{3+} concentration. This indicates that, beyond a

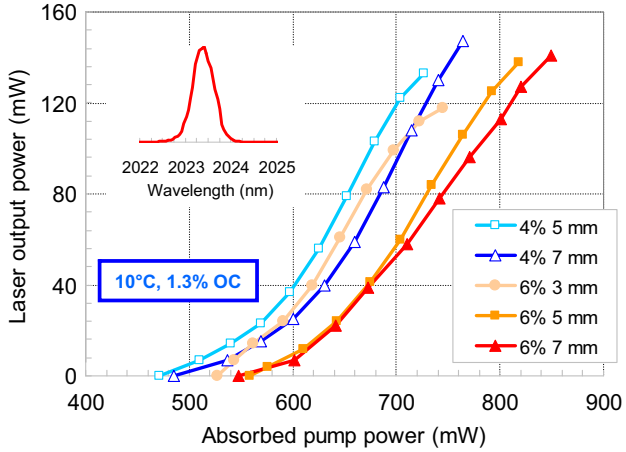

Fig. 2. Measured CW laser efficiency curves of the five Tm:LuAG crystals, 4% (5 and 7 mm) and 6% (3, 5, and 7 mm), using a 1.3% OC at a heatsink temperature of 10°C. The inset shows a representative free-running CW laser emission spectrum centered near 2023 nm.

Table 2. CW Performance of the Five Tm:LuAG Crystals at Water Temperatures of 10, 15, 20, and 25°C[a]

Tm^{3+} (at.%)	Length (mm)	Temp (°C)	Lasing Thres. (mW)	η (%)	η_{HP} (%)	P_{max} (mW)
4	7	10	513	64.6	76.6	147
		15	520	63	74	145
		20	534	62.6	73.6	139
		25	549	62.2	71.3	135
	5	10	486	62.7	75.5	133
		15	493	60.9	72.8	129
		20	498	60	71.4	125
		25	507	58.9	69.3	121
6	7	10	587	55.9	59.9	141
		15	580	49.7	52.6	139
		20	585	45.5	46.8	137
		25	582	41.7	43.4	129
	5	10	564	59.2	69.3	138
		15	571	57.2	66	134
		20	572	53.7	62.7	125
		25	591	53.7	61.4	121
	3	10	524	59.9	69.4	118
		15	523	62.2	72.7	112
		20	532	60	71.1	109
		25	542	57.5	66.7	103

[a]Listed are the lasing threshold (P_{th}), overall slope efficiency (η_{avg}), high-power slope efficiency (η_{HP}), and maximum output power (P_{max}).

certain optical depth, the benefit of stronger pump absorption is increasingly offset by reabsorption and passive loss.

The best overall performance was nevertheless obtained with the 4%, 7 mm crystal. At 10°C, it produced 147 mW with overall and high-power slope efficiencies of 64.6% and 76.6%, respectively. For pumping at approximately 1623 nm and lasing near 2023 nm, these values correspond to about 81% and 96% of the Stokes limit. Compared with the 4%, 5 mm crystal, the additional length therefore improved pump absorption and output extraction without introducing a significant efficiency penalty, although the shorter crystal retained the lower threshold.

A different trend appears for the 6% crystals. Increasing the length from 3 to 5 mm raised the maximum output power from 118 to 138 mW while leaving the slope efficiencies nearly unchanged. A further increase to 7 mm produced only a small additional power increase, to 141 mW, but reduced the overall and high-power slope efficiencies to 55.9% and 59.9%, respectively. Thus, at the higher Tm^{3+} concentration, the advantage of additional pump absorption is progressively outweighed by reabsorption and length-dependent loss.

The comparison therefore identifies the 4%, 7 mm crystal as the optimum sample under the present approximately 1 W pump-power and 1.3% output-coupling conditions. Among the tested samples, it also appears to be the most suitable candidate for moderate power scaling because it combines the highest efficiency with the most favorable temperature response. More generally, the results show that increasing crystal length is beneficial only until the gain from additional pump absorption is overtaken by reabsorption and passive-loss penalties. At substantially higher pump powers, longer crystals with lower Tm^{3+} concentrations may offer a more favorable scaling route by maintaining pump absorption while reducing concentration-dependent and thermal losses.

Table 3. Measured CW Output-Beam Quality Factors for the Investigated Tm:LuAG Crystals at a Crystal-Holder Temperature of 15°C

Tm^{3+} (at.%)	Length (mm)	M^2 Horizontal	M^2 Vertical
4	7	1.58	1.03
	5	1.35	1.11
6	7	1.42	1.16
	5	1.46	1.03
	3	1.15	1.01

Beyond output power and efficiency, beam quality is also important for assessing the practical utility and scaling potential of the system. The transverse beam quality was therefore measured near the maximum CW output-power level for all five crystals. As summarized in Table 3, M^2 ranged from 1.15 to 1.58 horizontally and from 1.01 to 1.16 vertically, indicating good spatial beam quality despite the strongly asymmetric pump beam, for which the corresponding M^2 values were 15 and 1.1. The consistently larger horizontal laser-beam M^2 values are compatible with the poorer pump-beam quality along this axis, although residual cavity astigmatism may also contribute. No systematic degradation of beam quality with crystal length or Tm^{3+} concentration was observed.

Having identified the optimum doping-length combination and confirmed its good beam quality, we next compare the present result with representative directly diode-pumped CW Tm:LuAG lasers. Table 4 includes systems employing conventional 785–790 nm pumping, high-brightness 681 nm pumping, and the present direct in-band pumping at 1621 nm. Conventional 785–790 nm pumping has produced substantially higher output powers, ranging from 3.04 to 8.5 W, with reported slope efficiencies of 25.3%–49.5% [28,29,40,41]. The corresponding high-power fiber-coupled multimode diodes provide estimated brightness values of 4−8 $mW/\mu m^2$. By comparison, the 681 nm tapered diode provided a much higher brightness of approximately 600 $mW/\mu m^2$ and generated 0.295 W with a slope efficiency of 46.4% [30].

The present 1621 nm single-emitter diode has an estimated brightness of approximately 23 $mW/\mu m^2$, lower than that of the 681 nm tapered diode but higher than the estimated values of the selected high-power fiber-coupled pump modules used in previous Tm studies. More importantly, it directly excites the $^3F_4$ upper laser level, reducing the quantum defect and thermal load without relying on cross relaxation. Although the available 1 W pump power limits the output to 0.147 W, the overall slope efficiency of 64.6% exceeds those of the directly diode-pumped Tm lasers listed in Table 4. The high-power slope efficiency reaches 76.6%, corresponding to approximately 96% of the Stokes limit. The present result therefore represents an efficiency benchmark for compact, low-power direct-diode pumping rather than an absolute power-scaling demonstration.

Table 4. Selected Directly Diode-Pumped CW Tm:LuAG Laser Results under Conventional (790 and 681 nm) and In-Band (1620 nm) Pumping

Pump Source	Diode Beam Quality	Diode Brightness (mW/μm^2)	P_{out} (W)	η (%)	Reference
20 W, 785 nm	~87	~4.2	3.04	25.3	[28]
1 W, 681 nm	~1.1 × 4.1	~600	0.295	46.4	[30]
20 W, 790 nm	~87	6.1	8.5	44.5	[29]
6.35 W, 785 nm	~44	5.3	0.62	12.8	[39]
9.6 W, 789 nm	~44	~8	4.42	49.5	[40]
20 W, 788 nm	—	—	4.91	25.4	[41]
1 W, 1621 nm	~1.1 × 15	~23	0.147	64.6/76.6	*

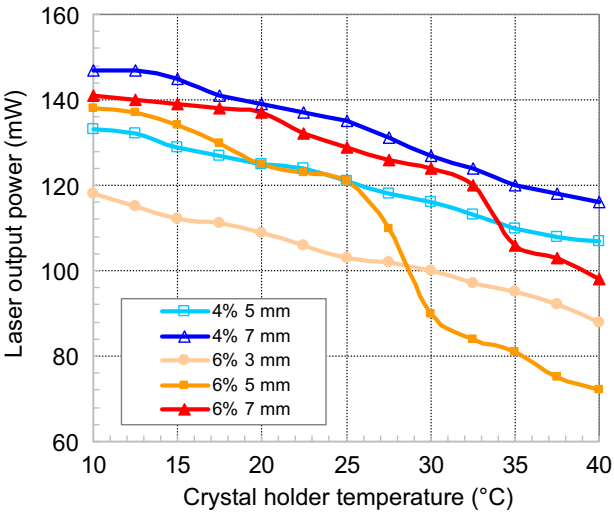

Fig. 3. Measured variation of CW output power with crystal-holder temperature for the five Tm:LuAG crystals. Data were taken with a 1.3% OC at the maximum incident pump power of 1 W.

B. Temperature Dependence of CW Lasing Performance

Figure 3 shows that the maximum CW output power decreases with increasing crystal-holder temperature for all five crystals, with a clear dependence on Tm^{3+} concentration. The 4% crystals exhibit the most stable response. In particular, the output power of the 7 mm sample decreases gradually from 147 mW at 10°C to 116 mW at 40°C. The 6% crystals show a stronger and less uniform roll-off, decreasing from 118 to 88 mW for the 3 mm sample, from 138 to 72 mW for the 5 mm sample, and from 141 to 98 mW for the 7 mm sample. The particularly steep decline of the 5 mm sample shows that the temperature response is not determined by crystal length alone, but by the combined balance among pump absorption, reabsorption, longitudinal inversion, and passive loss.

The overall slope efficiencies in Table 2 support the same concentration-dependent trend. Between 10 and 25°C, the overall slope efficiency decreases only from 64.6% to 62.2% for the 4%, 7 mm crystal and from 62.7% to 58.9% for the 4%, 5 mm crystal. The corresponding high-power slope efficiencies decrease from 76.6% to 71.3% and from 75.5% to 69.3%, respectively. The strongest efficiency degradation occurs in the 6%, 7 mm crystal, for which the overall and high-power slope efficiencies decrease from 55.9% to 41.7% and from 59.9% to 43.4%, respectively. Thus, the 4%, 7 mm crystal provides the best overall thermal tolerance, maintaining the highest output power together with the smallest decline in both overall and high-power slope efficiency among the longer crystals.

This behavior is consistent with the quasi-three-level nature of the $^3F_4 \rightarrow {}^3H_6$ transition. Increasing temperature raises the Boltzmann population of the terminal Stark levels in the $^3H_6$ manifold, increasing reabsorption at the laser wavelength and reducing the net gain. This penalty becomes stronger at higher Tm^{3+} concentration, while crystal length further modifies the accumulated reabsorption and longitudinal inversion profile. Although the present measurements do not separately quantify reabsorption or internal temperature gradients, the stronger degradation observed for the 6% samples is attributed primarily to their greater sensitivity to thermally enhanced reabsorption rather than to crystal length alone. Nevertheless, the low quantum defect of 1.6 μm in-band pumping limits the deposited heat relative to conventional 790 nm excitation, helping to preserve useful output power over the investigated temperature range.

C. Spectral Tuning and Dual Wavelength Operation

The spectral tuning and multi-wavelength operation of the in-band-pumped Tm laser were investigated using the 8-mm-thick, 25°-cut off-surface-optical-axis quartz BRF. Figure 4 shows the CW tuning curves measured with the 1.3% OC at a crystal-holder temperature of 15°C. All five crystals exhibit a similar spectral envelope, consisting of a weaker short-wavelength branch around 1960–1990 nm and a stronger gain region around 2015–2030 nm. This behavior is consistent with the calculated Tm gain cross-section spectra, which predict preferential positive gain near 2023 nm over a broad range of inversion levels [24,42]. Accordingly, the highest tuned output powers were obtained near 2025 nm. The 4%, 7 mm crystal produced the maximum value of 110 mW, followed by 100 mW from the 4%, 5 mm crystal and 75, 86, and 97 mW from the 6%, 3, 5, and 7 mm crystals, respectively.

Although the general spectral shape remained similar for all samples, the accessible tuning range depended strongly on the Tm^{3+} concentration and crystal length. The broadest range was obtained from the 4%, 5 mm crystal, covering 1937–2075 nm (138 nm), followed closely by 1944–2079 nm (135 nm) for the 4%, 7 mm crystal. The 6% crystals covered narrower ranges of 1956–2070, 1958–2076, and 1960–2076 nm for lengths of 3, 5, and 7 mm, respectively. The principal difference therefore occurs at the short-wavelength edge, where ground-state reabsorption is strongest. Increasing the Tm^{3+} concentration

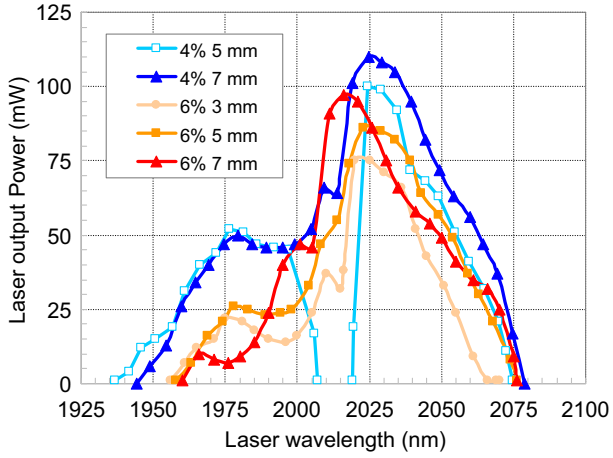

Fig. 4. CW tuning curves of the five Tm:LuAG crystals. The data were taken with a 1.3% OC at a crystal-holder temperature of 15°C.

Table 5. Summary of Wavelength Tuning Ranges and Representative Dual-Wavelength Pairs for the Five Tm:LuAG Crystals[a]

Tm^{3+} (at.%)	Length (mm)	Tuning Range (nm)	Δλ (nm)	Dual-λ Pair (nm)
4	7	1944–2079 (135)	106	1962 and 2068
4	5	1937–2075 (138)	90	1969 and 2059
6	7	1960–2076 (116)	34	2016 and 2050
6	5	1958–2076 (118)	34	2021 and 2055
6	3	1956–2070 (114)	71	1987 and 2058

[a]Δλ denotes the wavelength separation of the dual-wavelength pair.

raises the inversion required for positive gain and progressively shifts this edge toward longer wavelengths. The present 138 nm tuning range is narrower than those obtained in our earlier 681 nm-pumped Tm studies using the same BRF approach [43,44]. This reduction is attributed to the lower available gain under the present in-band-pumping conditions, particularly at the strongly reabsorbed short-wavelength edge, together with the limited 1 W pump power.

In addition to continuous single-wavelength tuning, stable dual-wavelength operation was observed at selected BRF orientations, as summarized in Table 5. At these orientations, two BRF transmission maxima could simultaneously fall within spectral regions of sufficient net gain, leading to stable dual-wavelength CW oscillation [44]. This behavior results from the multi-order transmission characteristics of the 8-mm-thick off-surface-optic-axis BRF [38]. Unlike a conventional BRF operating with an approximately fixed free spectral range, the off-surface-axis geometry allows different interference orders to contribute as the plate is rotated, resulting in strongly angle-dependent free spectral ranges and modulation depths [38]. In angular regions where the effective free spectral range is larger than or comparable to the usable laser-gain bandwidth, only one BRF transmission maximum satisfies the lasing condition, enabling continuous single-wavelength tuning (Fig. 4). At other orientations, higher-order transmission features with smaller free spectral ranges place two or more maxima within the broad Tm:LuAG gain spectrum (Figs. 5 and 6). When two such maxima experience comparable intracavity losses and the net gain

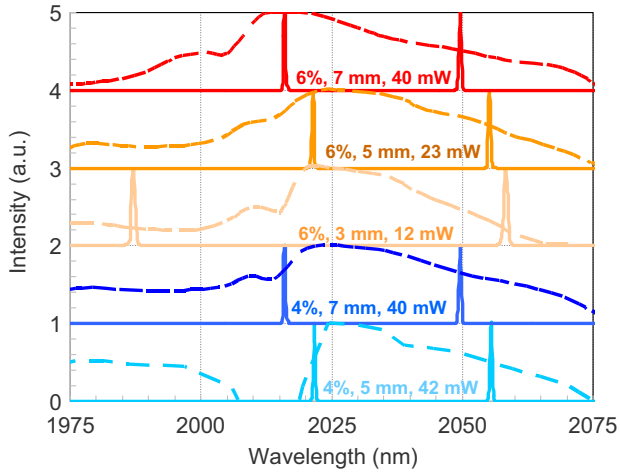

Fig. 5. Representative dual-wavelength emission spectra of the five Tm:LuAG crystals obtained at selected BRF angles. Dashed curves show the corresponding CW tuning envelopes, and labels indicate the crystal parameters and total two-color output power.

exceeds the lasing threshold at both wavelengths, simultaneous dual-wavelength oscillation occurs. The relative intensities of the two lines are then governed by the wavelength-dependent gain, reabsorption, BRF loss, and gain competition.

Representative dual-wavelength spectra corresponding to selected entries in Table 5 are shown in Fig. 5. The highest two-color output power was 42 mW from the 4%, 5 mm crystal, followed by 40 mW from both the 4%, 7 mm and 6%, 7 mm crystals. The representative wavelength separations ranged from 34 to 106 nm, with the largest separation obtained from the broadly tunable 4%, 7 mm crystal. Thus, the broader tuning envelopes of the 4% crystals also provided greater flexibility in selecting widely separated wavelength pairs.

Beyond dual-wavelength operation, the periodic transmission of the BRF also enabled three-line emission when three transmission maxima simultaneously overlapped regions of sufficient net gain. As shown in Fig. 6, the 6%, 5 mm crystal produced three resolved lines at approximately 2000, 2031, and 2067 nm, spanning 67 nm. These results demonstrate that the same compact resonator can access continuously tunable, dual-wavelength, and triple-wavelength CW regimes through rotation of a single intracavity BRF.

D. Passive Q-Switching with SESAM

Passive Q-switching was investigated at a water temperature of 15°C by replacing the flat HR end mirror with the CM3–SESAM arm described in Section 2. Stable, self-starting Q-switched operation was obtained with all five Tm crystals under the same cavity configuration. Figure 7 shows a representative pulse train and single-pulse profile for the 6%, 5 mm crystal. The pulses are clean and well separated, while the single-pulse trace exhibits a smooth temporal profile with an FWHM duration of 3.93 μs, without observable multi-pulsing or Q-switched mode-locking. The extracted Q-switching parameters are summarized in Table 6.

The 4%, 7 mm crystal provided the best pulse-shortening and peak-power performance, generating the shortest pulses

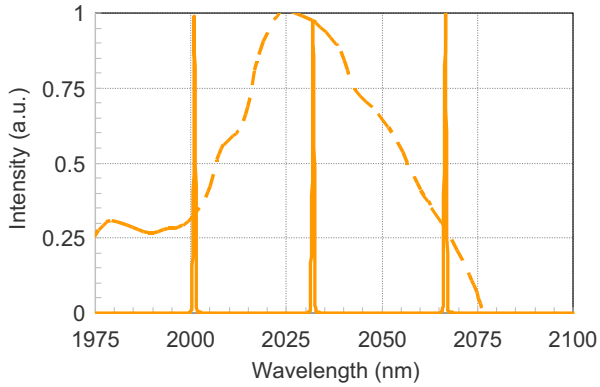

Fig. 6. Measured triple-wavelength (three-color) CW emission spectrum obtained with the 6%, 5 mm Tm:LuAG crystal, showing three simultaneously oscillating lines at 2000, 2031, and 2067 nm.

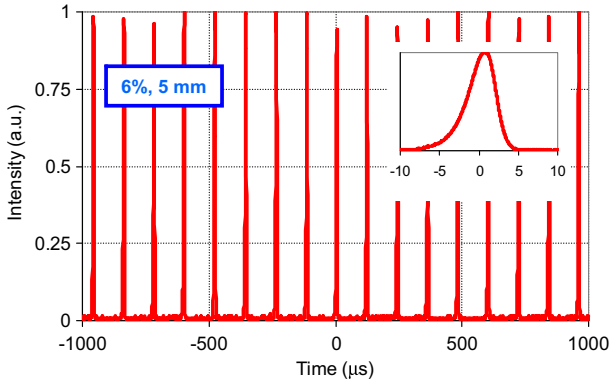

Fig. 7. Representative passive Q-switching results for the 6%, 5 mm Tm:LuAG crystal. Main panel: clean Q-switched pulse train. Inset: normalized single-pulse profile with an FWHM of 3.93 μs.

Table 6. Summary of Passive Q-Switching Characteristics for the Five Tm:LuAG Crystals at 15°C

Tm^{3+} (%)	L (mm)	P_{avg} (mW)	FWHM (μs)	f_{rep} (kHz)	P_{peak} (mW)	E_{pulse} (μJ)
4	7	8	1.99	7.12	564	1.12
4	5	20	5.42	16.28	226	1.23
6	7	17	3.04	15.73	355	1.08
6	5	12	3.93	8.44	362	1.42
6	3	11	5.54	10.74	184	1.02

of 1.99 μs and the highest peak power of 564 mW, together with a pulse energy of 1.12 μJ at 7.12 kHz. By comparison, the highest pulse energy of 1.42 μJ was obtained with the 6%, 5 mm crystal at 8.44 kHz, whereas the 4 %, 5 mm crystal produced the highest average Q-switched output power of 20 mW because of its higher repetition rate of 16.28 kHz. Thus, no single crystal optimized all Q-switching metrics. The superior CW gain margin of the 4%, 7 mm crystal favored faster pulse build-up and higher peak power, while the other configurations favored either stored pulse energy or repetition rate. These results show that the Q-switched performance is governed by the interplay among available gain, stored energy, pulse build-up time, and repetition rate. Although the present 1 W pump level, relatively long cavity, and 1.2% SESAM modulation depth limited the pulses to the μs regime, reliable self-starting operation from every crystal demonstrates that SESAM-based passive Q-switching is fully compatible with this compact in-band-pumped platform.

4. CONCLUSION

We demonstrated a compact in-band-pumped Tm:LuAG laser driven by a 1 W high-brightness single-emitter diode at 1.62 μm. A systematic comparison identified the 4%, 7 mm crystal as the optimum configuration at this pump level, delivering nearly 0.15 W of CW output with a local slope efficiency of 76.6%. The high pump brightness enabled efficient mode matching in a standard X-fold resonator and allowed the same simple, low-cost platform to support broad wavelength tuning, multi-wavelength emission, and SESAM Q-switching.

Looking beyond the present 1 W demonstration, further power scaling will require joint re-optimization of the pump mode, gain-medium geometry, Tm^{3+} concentration, crystal length, and thermal mounting, rather than simply increasing the pump power. At the present pump level, a relatively small pump mode is required to provide sufficient pump intensity for reaching the lasing threshold; therefore, the optimum pump-mode dimensions depend on the available pump power. At higher powers, a thinner crystal combined with an asymmetric pump mode expanded along one transverse axis could reduce the deposited heat density and, in an appropriately designed slab mount, promote approximately one-dimensional heat flow toward the cooled broad faces [45]. As high-brightness single-emitter diodes near 1.6 μm progress toward several watts, lower Tm^{3+} doping combined with a slightly longer crystal may maintain sufficient pump absorption while reducing concentration-dependent loss and thermal sensitivity. In contrast, ultrafast operation will likely benefit from a shorter crystal with lower reabsorption, passive loss, and dispersion. We hope that the present results provide initial practical design guidance for extending this approach toward higher-power CW, broadly tunable, and mode-locked operation.

Funding. Türkiye Bilimsel ve Teknolojik Araştırma Kurumu (119F308).

Disclosures. The authors declare no conflicts of interest.

Data availability. Data underlying the results presented in this paper are not publicly available at this time but may be obtained from the authors upon reasonable request.

REFERENCES

1. S. W. Henderson, P. J. M. Suni, C. P. Hale, *et al.*, "Coherent laser radar at 2 um using solid-state lasers," IEEE Trans. Geosci. Remote Sens. **31**, 4–15 (1993).
2. N. P. Barnes, "Eye-safe solid-state lasers for LIDAR applications," Proc. SPIE **0663**, 2–7 (1986).
3. K. Scholle, S. Lamrini, P. Koopmann, *et al.*, *2 μm Laser Sources and Their Possible Applications*, B. P. Pal, ed. (IntechOpen, 2010).
4. J. Yu, B. C. Trieu, M. Petros, *et al.*, "Advanced 2-micron solid-state laser for wind and CO_2 lidar applications," Proc. SPIE **6409**, 64091C (2006).
5. P. A. Budni, L. A. Pomeranz, M. L. Lemons, *et al.*, "Efficient mid-infrared laser using 1.9-mm pumped Ho:YAG and $ZnGeP_2$ optical parametric oscillators," J. Opt. Soc. Am. B **17**, 723–728 (2000).

6. I. F. Elder and M. J. P. Payne, "Lasing in diode-pumped Tm:YAP, Tm, Ho:YAP and Tm, Ho:YLF," Opt. Commun. **145**, 329–339 (1998).
7. S. A. Payne, L. L. Chase, L. K. Smith, *et al.*, "Infrared cross-section measurements for crystals doped with Er^{3+}, Tm^{3+}, and Ho^{3+}," IEEE J. Quantum Electron. **28**, 2619–2630 (1992).
8. R. C. Stoneman and L. Esterowitz, "Efficient, broadly tunable, laser-pumped Tm:YAG and Tm:YSGG cw lasers," Opt. Lett. **15**, 486–488 (1990).
9. S. So, J. I. MacKenzie, D. P. Shepherd, *et al.*, "A power-scaling strategy for longitudinally diode-pumped Tm:YLF lasers," Appl. Phys. B **84**, 389–393 (2006).
10. U. Demirbas, J. Thesinga, E. Beyatli, *et al.*, "Continuous-wave Tm:YLF laser with ultrabroad tuning (1772-2145 nm)," Opt. Express **30**, 41219–41239 (2022).
11. U. Demirbas, J. Thesinga, M. Kellert, *et al.*, "Temperature dependence of the fluorescence lifetime and emission cross section of Tm:YLF in the 78-300 K range," Opt. Mater. Express **12**, 4712–4732 (2022).
12. J. Kratochvíl, J. Šulc, and H. Jelínková, "Efficient 1.7 μm pumping of 2 μm thulium lasers," Opt. Lett. **48**, 4185–4188 (2023).
13. A. E. Troshin, V. E. Kisel, A. S. Yasukevich, *et al.*, "Spectroscopy and laser properties of Tm^{3+}: $KY(WO_4)_2$ crystal," Appl. Phys. B **86**, 287–292 (2007).
14. F. Trawi, M. Hamrouni, Z. Ertürk, *et al.*, "High-power, high-efficiency continuous-wave Tm:KYW laser with multimode in-band diode pumping," J. Eur. Opt. Soc. Publ. **22**, 44 (2026).
15. Y. L. Kalachev, V. A. Mihailov, V. V. Podreshetnikov, *et al.*, "The study of a Tm:YLF laser pumped by a Raman shifted Erbium fiber laser at 1678 nm," Opt. Commun. **284**, 3357–3360 (2011).
16. Y. Wang, D. Y. Shen, H. Chen, *et al.*, "Highly efficient Tm:YAG ceramic laser resonantly pumped at 1617 nm," Opt. Lett. **36**, 4485–4487 (2011).
17. W. Yao, F. Wu, Y. Zhao, *et al.*, "Highly efficient Tm:$CaYAlO_4$ laser in-band pumped by a Raman fiber laser at 1.7 μm," Appl. Opt. **55**, 3730–3733 (2016).
18. M. Tokurakawa, E. Fujita, and C. Krankel, "Kerr-lens mode-locked Tm^{3+}:Sc_2O_3 single-crystal laser in-band pumped by an Er:Yb fiber MOPA at 1611 nm," Opt. Lett. **42**, 3185–3188 (2017).
19. J.-J. Sun, Y. Chen, K. Zhang, *et al.*, "Efficient continuous wave and acousto-optical Q-switched Tm:Lu_2O_3 laser pumped by the laser diode at 1.7 μm," Infrared Phys. Technol. **116**, 103771 (2021).
20. W. Zhang, L. Li, S. Zhou, *et al.*, "High-efficiency diode-resonantly-pumped Tm:Lu_2O_3 ceramic laser with near diffraction-limited beam quality," J. Russ. Laser Res. **42**, 358–362 (2021).
21. R. Thouroude, A. Tyazhev, A. Hideur, *et al.*, "Widely tunable in-band-pumped Tm:CaF_2 laser," Opt. Lett. **45**, 4511–4514 (2020).
22. W. Huang, F. Wang, J. Wang, *et al.*, "Tm:Y_2O_3 ceramic laser in-band pumped at 1620 nm," in *Laser Congress (ASSL, LAC)* (Optica Publishing Group, 2021), paper AW1A.6.
23. X. M. Duan, X. S. Guo, B. Q. Yao, *et al.*, "Efficient Ho:CaF_2 laser intracavity-pumped by a Tm:LuAG laser in-band pumped at 1.6 μm," Laser Phys. Lett. **15**, 95802 (2018).
24. W. Zhang, L. Li, and H. Liang, "High-efficiency continuous-wave and LGS electro-optically Q-switched Tm: LuAG laser in-band pumped at 1623 nm," Opt. Laser Technol. **181**, 111947 (2025).
25. W. Zhang, L. Li, and H. Liang, "Efficient acousto-optically Q-switched Tm: LuAG laser end-pumped by a laser diode at 1.7 μm," Appl. Phys. B **131**, 65 (2025).
26. N. P. Barnes, M. G. Jani, and R. L. Hutcheson, "Diode-pumped, room-temperature Tm-LuAG laser," Appl. Opt. **34**, 4290–4294 (1995).
27. H. Kalaycioglu, A. Sennaroglu, A. Kurt, *et al.*, "Spectroscopic analysis of Tm^{3+}:LuAG," J. Phys. Condens. Matter **19**, 36208 (2007).
28. X. D. Xu, X. D. Wang, Z. F. Lin, *et al.*, "Crystal growth, spectroscopic and laser properties of Tm:LuAG crystal," Laser Phys. **19**, 2140–2143 (2009).
29. L. Guo, S. Z. Zhao, T. Li, *et al.*, "Diode-wing-pumped electro-optically Q-switched 2 μm laser with pulse energy scaling over ten millijoules," Opt. Express **26**, 17731–17738 (2018).
30. E. Beyatli, B. Sumpf, G. Erbert, *et al.*, "Efficient Tm:YAG and Tm:LuAG lasers pumped by 681 nm tapered diodes," Appl. Opt. **58**, 2973–2980 (2019).
31. C. Liu, K. Yang, S. Zhao, *et al.*, "88ns multi-millijoule $LiNbO_3$ electro-optically Q-switched Tm:LuAG laser," Opt. Commun. **355**, 167–171 (2015).
32. C. Luan, K. J. Yang, J. Zhao, *et al.*, "WS_2 as a saturable absorber for Q-switched 2 micron lasers," Opt. Lett. **41**, 3783–3786 (2016).
33. L. Wu, D. Li, S. Zhao, *et al.*, "Passive Q-switching with GaAs or Bi-doped GaAs saturable absorber in Tm:LuAG laser operating at 2 μm wavelength," Opt. Express **23**, 15469–15476 (2015).
34. R. Sun, C. Chen, W.-J. Ling, *et al.*, "Watt-level passively Q-switched mode-locked Tm:LuAG laser with graphene oxide SA," Acta Phys. Sin. **68**, 104207 (2019).
35. C. Luan, K. Yang, J. Zhao, *et al.*, "Diode-pumped mode-locked Tm:LuAG laser at 2 μm based on GaSb-SESAM," Opt. Lett. **42**, 839–842 (2017).
36. T. Feng, K. Yang, J. Zhao, *et al.*, "1.21 W passively mode-locked Tm:LuAG laser," Opt. Express **23**, 11819–11825 (2015).
37. H. Wenzel, B. Sumpf, and G. Erbert, "High-brightness diode lasers," C. R. Phys. **4**, 649–661 (2003).
38. U. Demirbas, "Off-surface optic axis birefringent filters for smooth tuning of broadband lasers," Appl. Opt. **56**, 7815–7825 (2017).
39. L. Wang, C. Gao, M. Gao, *et al.*, "Diode-pumped 2 μm tunable single-frequency Tm:LuAG laser with intracavity, etalons," Appl. Opt. **52**, 1272–1275 (2013).
40. T. Feng, K. Yang, S. Zhao, *et al.*, "Efficient CW dual-wavelength and passively *Q*-switched Tm:LuAG lasers," IEEE Photonics Technol. Lett. **27**, 7–10 (2015).
41. C. Wu, Y. Ju, Y. Li, *et al.*, "Diode-pumped Tm:LuAG laser at room temperature," Chin. Opt. Lett. **6**, 415–416 (2008).
42. Y. C. Wang, R. J. Lan, X. Mateos, *et al.*, "Thulium doped LuAG ceramics for passively mode locked lasers," Opt. Express **25**, 7084–7091 (2017).
43. F. Kaya, H. Bilici, B. Sumpf, *et al.*, "Crystal-length optimization in 681-nm pumped Tm:YAG and Tm:LuAG lasers: from low threshold to SESAM Q-switching," Opt. Commun. **616**, 133364 (2026).
44. E. Beyatli and U. Demirbas, "Widely tunable dual-wavelength operation of Tm:YLF, Tm:LuAG, and Tm:YAG lasers using off-surface optic axis birefringent filters," Appl. Opt. **57**, 6679–6686 (2018).
45. D. Kopf, J. A. Derau, U. Keller, *et al.*, "400-mW continuous-wave diode-pumped Cr-LiSAF laser-based on a power-scalable concept," Opt. Lett. **20**, 1782–1784 (1995).